Asteroid 2867 Steins. III. Spitzer Space Telescope observations, size determination, and thermal properties

Philippe Lamy, Laurent Jorda, Sonia Fornasier, Olivier Groussin, Maria Antonella Barucci, Jorge M. Carvano, Elisabetta Dotto, Marcello Fulchignoni, Imre Toth

▶ **To cite this version:**

Philippe Lamy, Laurent Jorda, Sonia Fornasier, Olivier Groussin, Maria Antonella Barucci, et al.. Asteroid 2867 Steins. III. Spitzer Space Telescope observations, size determination, and thermal properties. Astronomy and Astrophysics - A&A, 2008, 487, pp.1187-1193. 10.1051/0004-6361:20078996 . hal-03730677

HAL Id: hal-03730677
https://hal.science/hal-03730677

Submitted on 13 Oct 2022

HAL is a multi-disciplinary open access archive for the deposit and dissemination of scientific research documents, whether they are published or not. The documents may come from teaching and research institutions in France or abroad, or from public or private research centers.

L'archive ouverte pluridisciplinaire **HAL**, est destinée au dépôt et à la diffusion de documents scientifiques de niveau recherche, publiés ou non, émanant des établissements d'enseignement et de recherche français ou étrangers, des laboratoires publics ou privés.

A&A 487, 1187–1193 (2008)
DOI: 10.1051/0004-6361:20078996
© ESO 2008

Astronomy & Astrophysics

Asteroid 2867 Steins

III. Spitzer Space Telescope observations, size determination, and thermal properties

P. L. Lamy[1], L. Jorda[1], S. Fornasier[2,3], O. Groussin[1], M. A. Barucci[2], J. Carvano[4], E. Dotto[5], M. Fulchignoni[2,3], and I. Toth[1,6]

[1] Laboratoire d'Astrophysique de Marseille, UMR6110 CNRS/Université de Provence, Technopôle de Marseille-Etoile, 38 rue Frédéric Joliot-Curie, 13388 Marseille Cedex 13, France
e-mail: philippe.lamy@oamp.fr
[2] LESIA, Observatoire de Paris, 92195 Meudon Principal Cedex, France
[3] Université de Paris 7 Denis Diderot, France
[4] Observatorio National de Rio de Janeiro, Brazil
[5] INAF - Osservatorio Astronomico di Roma, via Frascati 33, 00040 Monteporzio Catone (Roma), Italy
[6] Konkoly Observatory, PO Box 67, 1525, Hungary

Received 5 November 2007 / Accepted 25 May 2008

ABSTRACT

Context. Asteroid 2867 Steins is the first target of the Rosetta space mission with a flyby scheduled in September 2008.
Aims. An early characterization is needed to optimize the flyby parameters and the science operations, and to maximize the scientific return.
Methods. We used the infrared spectrograph (IRS) of the Spitzer Space Telescope (SST) to obtain 14 spectra ranging from 5.2 to 38.0 μm, and to sample the rotational period of the asteroid. The observations were performed on 22 November 2005, when the asteroid was 2.13 AU from the Sun, 1.60 AU from the SST, and at a phase angle of 27.2°. They were interpreted using a standard thermal model incorporating the thermal inertia.
Results. The solution for a spherical shape leads to an effective radius r_n = 2.46 ± 0.20 km and a thermal inertia I = 150 ± 60 J K^{-1} m^{-2} s$^{-1/2}$, for a beaming factor between 0.8 and 1.0. The geometric albedo is then constrained by visible photometry to p_R = 0.31 ± 0.05 and p_V = 0.27 ± 0.04 when using a linear phase function. The $H-G$ phase law, which includes an opposition effect, leads to larger values of the albedo, $p_R(H-G)$ = 0.40 ± 0.07 and $p_V(H-G)$ = 0.34 ± 0.06. The solution for our 3-dimensional shape model has overall dimensions of 5.73 ± 0.52 × 4.95 ± 0.45 × 4.58 ± 0.41 km.

Key words. minor planets, asteroids – techniques: image processing

1. Introduction

This article on asteroid 2867 Steins, the first target of the Rosetta space mission, is the third in a series of four companion articles.

- Article I (Jorda et al. 2008) describes the lightcurve data obtained with the OSIRIS narrow angle camera (NAC) aboard the Rosetta spacecraft itself, and discusses photometric properties (color, phase function).
- Article II (Lamy et al. 2008) presents multi-telescope visible observations, shape reconstruction and rotational state.
- This present Article (III) presents thermal radiometry obtained with the Spitzer Space Telescope (SST), and focuses on the size, albedo and thermal properties.
- Article IV (Barucci et al. 2008) reports on the thermal emissivity, and discusses the mineralogical composition and taxonomic classification.

The reader is referred to Article I for the general context of the investigation and for a summary of our present knowledge of asteroid Steins. The present article is organized as follows: We first present the SST observations of 2867 Steins, the data reduction, and the set of resulting spectral energy distributions (SEDs). We then introduce the thermal model implemented to analyze the above results, and discuss the involved parameters. We first consider a spherical model of the asteroid, determine its size, its albedo by combining with visible photometry, and constrain its thermal inertia. We finally scale our three-dimensional shape model (Lamy et al. 2008, Article II) by adjusting the calculated thermal light curve to the observed one.

2. Observations with the SST

2.1. Observations

There were only two visibility windows of about 20 days each to observe 2867 Steins with the SST during cycle 2 because of the restriction on solar elongation (80−120°). The scheduled window was chosen so as to maximize the thermal flux expected from Steins and reach the best signal-over-noise ratio. The observations took place on 22 November 2005, the asteroid being at a heliocentric distance of 2.13 AU, at a distance from the SST of 1.60 AU and at a solar phase angle of 27.2°. We used the infrared

Table 1. Observational circumstances for the observations of 2867 Steins with the SST on 22 November 2005.

Target (set)	UT_{start} (hh:mm:ss)	UT_{end} (hh:mm:ss)	r_h (AU)	Δ (AU)	α (°)
Steins [01]	06:23:56	06:31:05	2.1304590	1.6021574	27.19
Steins [02]	07:02:50	07:09:59	2.1304959	1.6024785	27.20
Steins [03]	07:38:07	07:45:16	2.1305283	1.6027595	27.20
Steins [04]	08:12:58	08:20:07	2.1305606	1.6030406	27.20
Steins [05]	08:34:48	08:41:57	2.1305791	1.6032012	27.20
Steins [06]	09:07:43	09:14:52	2.1306069	1.6034421	27.20
Steins [07]	09:31:58	09:39:06	2.1306299	1.6036429	27.20
Steins [08]	10:03:53	10:11:01	2.1306622	1.6039240	27.21
Steins [09]	10:38:03	10:45:12	2.1306945	1.6042051	27.21
Steins [10]	11:04:26	11:11:34	2.1307176	1.6044060	27.21
Steins [11]	11:35:06	11:42:15	2.1307454	1.6046471	27.21
Steins [12]	12:12:03	12:19:12	2.1307777	1.6049283	27.21
Steins [13]	12:36:18	12:43:26	2.1308008	1.6051292	27.21
Steins [14]	13:11:21	13:18:29	2.1308332	1.6054105	27.22

r_h, Δ: Distances from Steins to respectively the Sun and the SST, α: solar phase angle as seen from the SST.

spectrograph (IRS) in the low-resolution mode ($R = \lambda/\Delta\lambda \sim 64-128$), which covers the wavelength range 5.2−38 μm in four long-slit segments: the short wavelength, 2nd order (SL2, from 5.2 to 8.5 μm); the short wavelength, 1st order (SL1, from 7.4 to 14.2 μm); the long wavelength, 2nd order (LL2, from 14.0 to 21.5 μm); and the long wavelength, 1st order (LL1, from 19.5 to 38.0 μm). The observational sequence was repeated 14 times at time interval of 30 min from UT = 6:23 to UT = 13:18 in order to fully sample its rotational period of ~6 h. Geometric conditions for these 14 visits are reported in Table 1. All spectra were acquired with a single ramp of 14.68 s, except for the SL1 segment for which we used a 6.29 s ramp. The pointing of the target was performed using the ephemeris derived from the Horizon database maintained by the Solar System Dynamics Group at the Jet Propulsion Laboratory. In addition, we used the blue peak-up camera to obtain images at 16 μm, and place the asteroid image inside the slits with high accuracy. This was indeed required as Steins is a moving target, and as the SL mode has slits of only 3.6 arcsec wide, while for the LL mode the slits are larger (10.6 arcsec). Details about the SST and its infrared spectrograph can be found in Werner et al. (2004) and in the Spitzer observer's manual (http://ssc.spitzer.caltech.edu/documents/SOM/irs60.pdf).

2.2. Data reduction

The science data coming from the IRS instrument are received and processed at the Spitzer Space Center (SSC). We used the basic calibrated data (BCD) produced by an automated data reduction pipeline (version S13.0) that includes cosmic rays removal, dark current subtraction, collapsing cubes to two-dimensional flux images by fitting ramp slopes, flat fielding, and stray light correction. A detailed description of the pipeline reduction steps can be found in Houck et al. (2004), and in the IRS Spitzer observer's manual – IRS pipeline handbook (http://ssc.spitzer.caltech.edu/irs/dh/). The calibration dataset was provided by the SSC together with the scientific data.

The sky subtraction is not performed by the automated pipeline. The background of the IRS images is dominated by the zodiacal cloud with a minor component from the interstellar medium. We performed the sky correction by differencing the 2 Nods. positions available for the observations in each spectral segment, following a standard "chopping" technique usually applied to ground-based infrared observations. The size of the offset (one third of the slit length) is large enough so that compact objects have no overlapping pixels in the two dispersed images.

We extracted the one-dimensional spectra in the four IRS segments using SPICE, the Spitzer IRS Custom Extraction software in JAVA language (version 1.3). The extraction pipeline takes as input the two-dimensional background subtracted BCD image in FITS format. Each BCD has an associated uncertainty and bitmask file, which indicates individual pixel status.

The SPICE spectral extraction thread consists of four modules:

1. It creates wavelength-collapsed average spatial profile of the slit used in the observation.
2. The location of the peak in the PROFILE output is identified for the point source extraction.
3. The spectrum is extracted (flux is in electron/s) along the RIDGE location in accordance with the wavelength-dependent point spread function (PSF) and the spectral profile. It must be noted that the source spectrum incident on the array is not rectilinear in either the spectral or cross-dispersed direction. As a result, the EXTRACT module does not extract whole pixels, but rather subdivides the array into a network of polygon-shaped sampling elements referred to as "pseudo-rectangles", which do not necessarily overlap the rectangular pixel grid. These elements allow Nyquist sampling of spectra in the dispersion direction. Extraction is performed by calculating the signal that falls within the boundary of the "pseudo-rectangles". Light is assumed to be evenly distributed within a pixel for purposes of calculating fractional contribution.
4. The software applies photometric tuning and flux conversion coefficients to the 1D spectra, getting a flux in Jansky. This module also corrects the slope and curvature of each order by applying a polynomial coefficients based on the calibration dataset. This correction is based on an order-by-order comparison of calibration data to standard star model spectra.

2.3. Uncertainties

According to the SPICE data handbook, pointing uncertanties with high accuracy peak-up will result in photometric uncertainties of ±2% within a given nod position. However mismatches between different low-resolution modules may be as large as 5%. "Jumps" in flux between the SL and LL spectral orders for a source observed with both modules are typically less than 5%, once background emissions from zodiacal dust and cirrus have been removed. Note that the point source calibration is based on an average of multiple observations of the standard star. Due to differences in the fluxes of each nod, an individual observation may show other mismatches between SL and LL.

2.4. Results

The fourteen SEDs over the full spectral range 5−38 μm are displayed in Fig. 1. The fluxes are much less than anticipated as the asteroid turns out to be appreciably smaller than predicted at that time. The signal-over-noise ratio is therefore not optimum, and seriously degraded beyond about 34 μm.

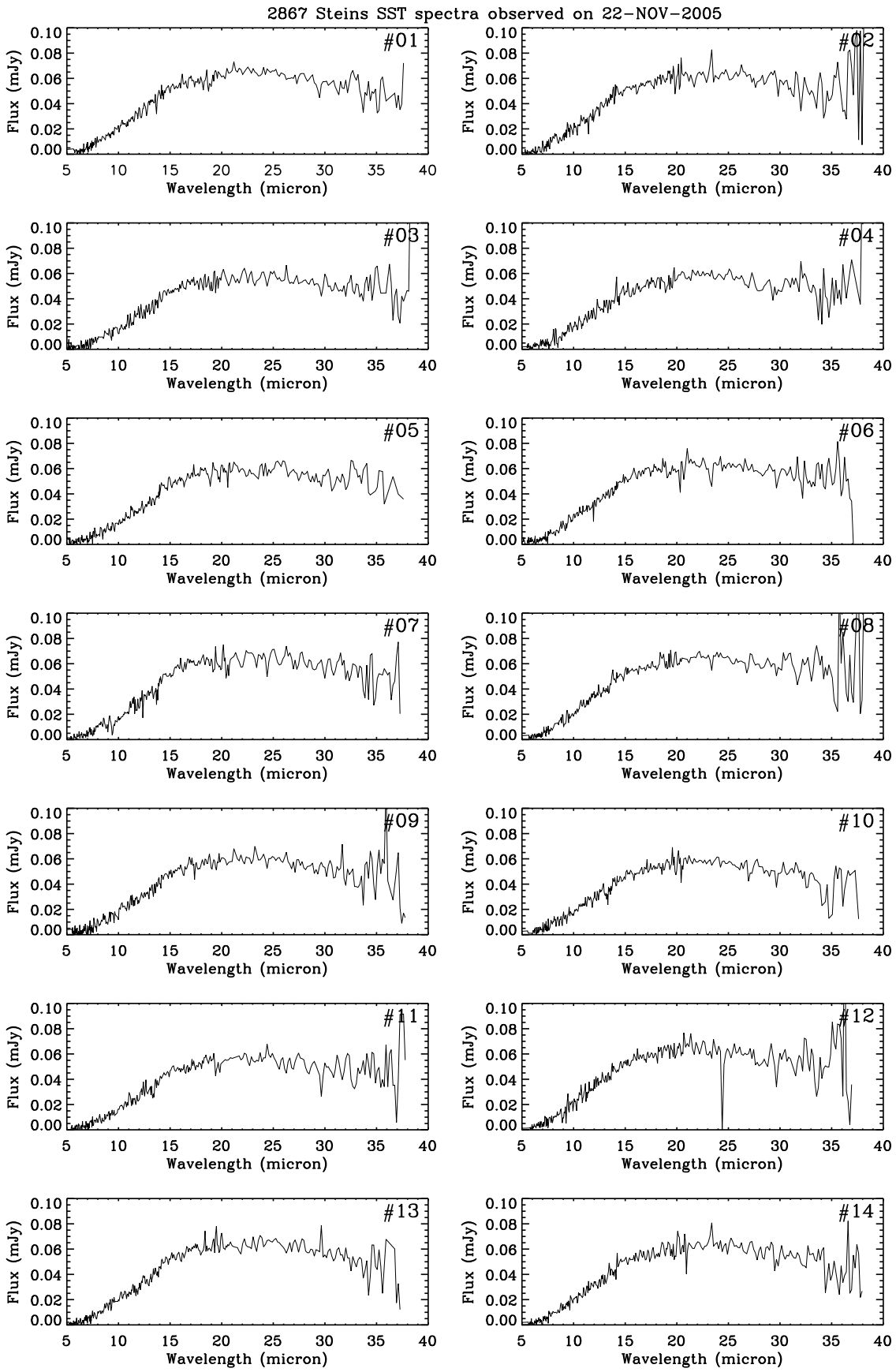

Fig. 1. The fourteen SEDs over the full spectral range 5−38 μm.

3. Analysis and interpretation

3.1. Thermal model

The interpretation of the infrared data requires a thermal model, which decribes the energy balance on the surface between the flux received from the Sun, the re-radiated flux, and the heat conduction into the asteroid. We consider two models for the shape of the asteroid: i) a sphere for a simple and robust solution; and ii) the shape derived from a set of light curves presented by Lamy et al. (2008, Article II). Their surface is divided into ~1000 facets. The surface energy balance for each facet with index i is given by Eq. (1):

$$(1 - p_V q)\frac{F_{\rm sun}}{r_{\rm h}^2} v_i \cos(z_i) = \eta\epsilon\sigma T_i^4 + \kappa\frac{\partial T_i}{\partial x}\bigg|_{x=0} \quad (1)$$

where p_V is the geometric albedo in the V band; q is the phase integral in the same band; $F_{\rm sun}$ [W m^{-2}] is the solar constant; $r_{\rm h}$ [AU] is the heliocentric distance; v_i is the illumination factor of facet i ($v_i = 1$ if the facet is illuminated and $v_i = 0$ if the facet is in shadow); z_i is the zenithal angle of facet i; η is the beaming factor introduced by Lebofsky & Spencer (1989); T_i [K] is the surface temperature of facet i; κ [W m^{-1} K^{-1}] is the thermal conductivity and x measures the depth. Numerical values for the parameters will be discussed in Sect. 3.1.2.

As the asteroid rotates around its spin axis, the values of z_i change, and the heat equation conduction is computed for each facet. We consider the one-dimensional (x) time-dependent (t) equation for the heat conduction:

$$\rho C\frac{\partial T_i(x,t)}{\partial t} = \frac{\partial}{\partial x}\left(\kappa\frac{\partial T_i(x,t)}{\partial x}\right) \quad (2)$$

where ρ [kg/m^3] is the bulk density, and C [J/kg/K] is the specific heat capacity of the asteroid. We solve Eqs. (1) and (2) using a method similar to that of Spencer et al. (1989), and described in Groussin et al. (2004). We use a time step of 86 s, which is small enough compared to the rotation period (6.0 h) to insure relaxation of the numerical solution in 30 rotations. As a result, we obtain the temperature of each facet as a function of time, over one period of rotation. From this temperature profile, we calculate the infrared flux F_i from each facet of index i as a function of time using Eq. (3):

$$F_i(\lambda) = \frac{\epsilon}{\Delta^2} B(\lambda, T_i) u_i \cos(w_i)\gamma {\rm d}S_i \quad (3)$$

where λ [μm] is the wavelength; Δ [km] the distance to the observer (SST in our case); B is the Planck function; u_i is the view factor between facet i and the observer ($u_i = 1$ if the observer see the facet; $u_i = 0$ otherwize); w_i is the phase angle of the facet i; γ is an arbitrary scaling factor applied to the shape model; and ${\rm d}S_i$ is the surface area of facet i. The total flux received by the observer is the sum of the individual fluxes F_i of all facets of the shape model. It is computed at different wavelengths λ to construct the spectral energy distribution.

As illustrated in Fig. 2, Steins has a red spectrum, and the assumption of a constant geometric albedo p_V implicit in Eq. (1) is not strictly valid as p is a function of the wavelength λ. Assuming a reasonable extrapolation beyond the 0.2−2.4 μm interval for the reflectivity $S(\lambda)$, we can rewrite Eq. (1) as:

$$\int_\lambda (1 - p_V S(\lambda) q)\frac{F_{\rm sun}(\lambda)}{r_{\rm h}^2} v_i \cos(z_i) = \eta\epsilon\sigma T_i^4 + \kappa\frac{\partial T_i}{\partial x}\bigg|_{x=0} \quad (4)$$

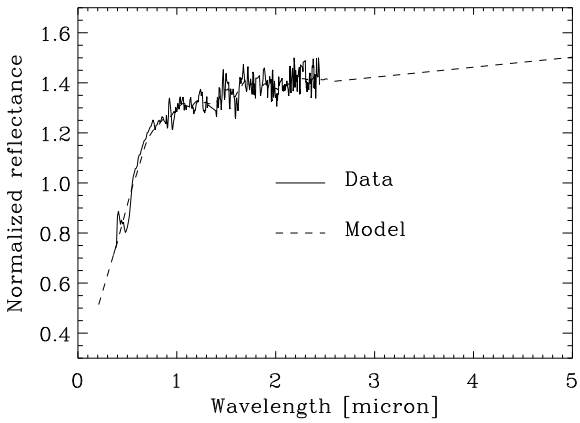

Fig. 2. The relative reflectivity of Steins from 0.2 to 5.0 micron. The solid line corresponds to the IRTF data from Barucci et al. (2005). The dotted line corresponds to an extrapolation of the data assuming the same constant slope as determined in the interval 1.0 to 2.5 μm.

where $S(\lambda)$ is normalized to 1 at the center of the V band (0.55 μm), and displayed in Fig. 2. The difference between the two methods – a constant albedo, on the one hand, and the above variation $p_V S(\lambda)$ on the other hand – has a negligible effect on the determination of the radius (<2%) and of the albedo (<3%).

3.2. Parameters of the thermal model

Our model has six free parameters: the infrared emissivity ϵ, the phase integral q, the scaling coefficient γ, the geometric albedo p_V, the beaming factor η, and the thermal inertia I. Among these six parameters, we consider that two of them ϵ and q can be reasonably assumed, while the other four γ, η, p_V, and I must be determined or constrained from the observational results.

The infrared emissivity ϵ is taken equal to 0.95, the middle point of the interval 0.9−1.0 always quoted in the literature. As the interval is very small and the value near 1.0, this uncertainty has a negligible influence on the calculated thermal flux.

The phase integral q is given by the following integral

$$q = 2\int_{0^\pi} \Phi(\alpha)\cos(\alpha){\rm d}\alpha \quad (5)$$

where $\Phi(\alpha)$, the normalized phase curve, describes the dependence of the scattered radiation upon phase angle. Steins is an E-type asteroid for which the value of q is unknown. We note that S- and C-types asteroids have rather similar phase curves (Helfenstein & Veverka 1989; Buratti et al. 2004) leading to a common phase integral $q = 0.28$, a value which we presently adopt for Steins. It is further intermediate between a minimum of $q = 0.2$ determined for Ida (Helfenstein et al. 1996) and a maximum of $q = 0.4$ for Deimos (Thomas et al. 1996).

The parameter γ only scales the SED, and directly controls the size of the asteroid. As a consequence, it can be independently determined for each combination of [η, p_V, I].

The beaming factor η follows the strict definition given by Lagerros (1998), and therefore only reflects the influence of surface roughness which produces an anisotropic thermal emission. Theoretically, η ranges from 0 to 1, but in practice it must be larger than 0.7 to avoid unrealistic roughness, with rms slopes exceeding 1 (Lagerros 1998). We point out that in the classical thermal models, such as the refined STM of Lebofsky et al. (1986) and the NEATM of Harris (1998), the beaming factor

globally accounts for different physical effects (including the thermal inertia) and may be larger than 1. Indeed, the empirical relationship $\eta = 0.81 + 0.01\alpha$ (where α is the phase angle) proposed by Delbó et al. (2003) yields $\eta = 1.08$ in our case. In this study, we consider three values: $\eta = 0.8$, 0.9 and 1.0.

Finally we sample the whole range [0, 1] of geometric albedo p_V with a step of 0.05, and the range [0, 400] J K^{-1} m^{-2} s$^{-1/2}$ of thermal inertia I with eight values $I = 0$, 25, 50, 100, 150, 200, 300, 400 J K^{-1} m^{-2} s$^{-1/2}$.

3.3. Solution for the spherical shape

3.3.1. Thermal parameters

The three parameters η, p_V, and I, as well as the shape of the asteroid (through the temperature distribution at its surface), control the spectral distribution of energy. On the contrary, γ is a parameter scaling the infrared flux, and has no influence on the shape of the SED. Obviously, we have more unknowns than constraints, and the problem must be simplified with proper assumptions. We first consider a spherical shape model to obtain a robust determination of the parameters. Fortunately, with axial ratios $a/b = 1.17$ and $a/c = 1.25$ (Article II), 2867 Steins is rather spherical so this assumption is valid. Consistent with this approach, we average the fourteen SEDs, which sample the rotational period of the asteroid. This is further justified by the lack of significant differences between the individual SEDs as also pointed out by Barucci et al. (2007), and has the advantage of improving the signal-to-noise ratio. Then, our procedure consists in setting η to one of the selected three values (0.8, 0.9, 1.0), and adjusting the calculated SED produced by our thermal model to the observed average SED for different combinations of p_V and I: for each selected value of I, we determine the corresponding value of p_V, which minimizes the differences based on the least square method. The results are illustrated in Fig. 3. At this stage, it is not possible to determine a unique solution, and very different combinations of parameters yields equally good fits to the data. However, extreme values of albedo such as $p_V < 0.2$ or $p_V > 0.6$, and thermal inertia such as $I \sim 0$ J K^{-1} m^{-2} s$^{-1/2}$ can be safely ruled out for an E-type asteroid. As an illustration of a possible realistic solution, we display in Fig. 4 the case corresponding to $\eta = 0.9$, $I = 150$ and $p_V = 0.3$. Residuals are less than 10% between 10 and 33 μm, indicating a good agreement between the model and the data. They are however larger at shorter wavelengths because the flux is low, and at longer wavelengths because of the poor signal-to-noise ratio.

3.3.2. Size of the asteroid

We next determine the radius of the spherical model by integrating both the observed average SED and the calculated one between 5 and 33 μm, the ratio of the two fluxes yielding the scaling parameter γ. The results for different combinations of parameters are presented in Table 2. Clearly, the mean radius of the asteroid is very well constrained between 2.38 and 2.53 km, whatever the values of η, p_V, I, emphasizing the strength of the approach which relies on thermal measurements to determine the size. Further imposing a realistic range of albedo of 0.2 to 0.6 for an E-type asteroid, the mean radius is further constrained to the interval 2.43 to 2.49 km, that is 2.46 ± 0.03 km. On the contrary, this method leaves the couple of parameters $[p_V, I]$ poorly constrained. Fortunately, the albedo can be determined from visible observations once the size is known as explained below.

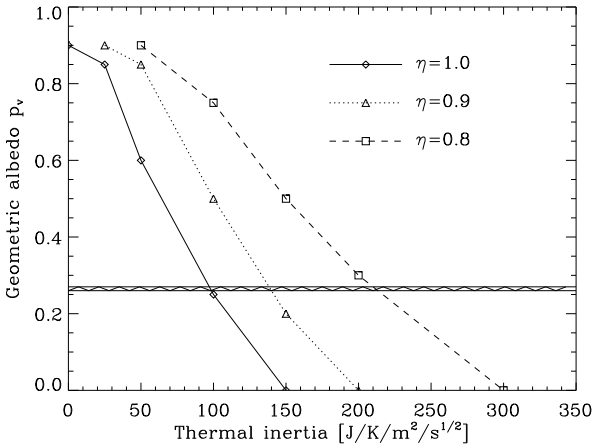

Fig. 3. Geometric albedo p_V in the V band as a function of thermal inertia I (J K^{-1} m^{-2} s$^{-1/2}$) for different values of the beaming factor η. The hatched region corresponds to the geometric albedo derived from this work.

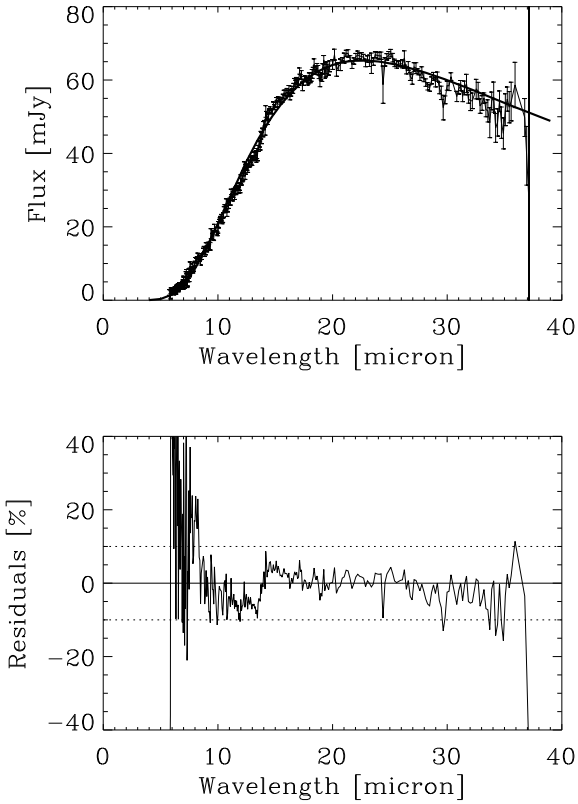

Fig. 4. Comparison between the observed (average) SED and that calculated for the following parameters of the thermal model: $\eta = 0.9$, $I = 150$ J K^{-1} m^{-2} s$^{-1/2}$ and $p_V = 0.3$ (solid line). The upper panel displays the SEDs (error bar = 1σ of the average), and the lower panel the residuals.

3.3.3. Albedo

The standard formula relating magnitudes to cross-sections, originally devised by Russell (1916) for asteroids observed at large phase angles, has been conveniently reformulated by Jewitt (1991). It allows us to calculate the geometric albedo p in a given photometric band for the different values of the mean radius listed in Table 2. We use the reduced magnitudes $R(1, 1, 0)$ given by Jorda et al. (2007, Article I), take the mean of their

Table 2. Physical properties of asteroid 2867 Steins.

η	I	p_V	r_n	p_R	$p_R(H-G)$	p_V	$p_V(H-G)$
1.0	0	0.90	2.46	0.31	0.27	0.40	0.34
1.0	25	0.85	2.53	0.29	0.25	0.37	0.32
1.0	50	0.60	2.49	0.30	0.26	0.39	0.33
1.0	100	0.25	2.48	0.31	0.26	0.39	0.33
1.0	150	0.00	2.48	0.31	0.26	0.39	0.33
0.9	25	0.90	2.43	0.32	0.27	0.41	0.35
0.9	50	0.85	2.49	0.30	0.26	0.39	0.33
0.9	100	0.50	2.47	0.31	0.26	0.39	0.34
0.9	150	0.20	2.44	0.32	0.27	0.40	0.34
0.9	200	0.00	2.44	0.32	0.27	0.40	0.34
0.8	50	0.90	2.38	0.33	0.28	0.42	0.36
0.8	100	0.75	2.46	0.31	0.27	0.40	0.34
0.8	150	0.50	2.44	0.32	0.27	0.40	0.34
0.8	200	0.30	2.43	0.32	0.27	0.41	0.35
0.8	300	0.00	2.42	0.32	0.28	0.41	0.35

η: Beaming factor, I: thermal inertia (J K^{-1} m^{-2} s$^{-1/2}$) that gives the best fit to the SED, p_V: geometric albedo for the V band that gives the best fit to the SED, r_n: mean radius (km) of the asteroid (see text), p_R: geometric albedo in the R band using a linear phase law, $p_R(H-G)$: geometric albedo in the R band using a (H,G) phase law, p_V: geometric albedo in the V band using a linear phase law, $p_V(H-G)$: geometric albedo in the V band using a (H,G) phase law.

extreme values corresponding to the maximum and minimum cross-sections, and consider their two cases.

1. The linear phase law with a coefficient $\beta = 0.025$ mag/deg and $R(1,1,0) = 13.095 \pm 0.036$. In this case, any opposition effect is ignored and the resulting albedo is representative of the global photometric properties of the asteroid consistent with Eq. (1); it is also consistent with the definition of the geometric albedo, which relies on the comparison with a lambertian diffuser (Hanner et al. 1980). From the size range found in the above section, we derive a range of albedo $p_R = 0.30$–0.32.
2. The (H,G) phase law with a coefficient $G = 0.35$ mag/deg and $H = R(1,1,0) = 12.84 \pm 0.07$. In this case, the opposition effect is introduced and artificially increases the albedo. We report the corresponding result since it is of standard use for the classification of asteroids but emphasize that: i) the opposition surge of 0.25 mag, although typical of E-type asteroids, is not really constrained because data are presently lacking at phase angles below 7°; and ii) the resulting albedo is irrelevant to the thermal balance as described by Eq. (1). From the size range found in the above section, we derive a range of albedo $p_R(H-G) = 0.39$–0.41.

Further, using the color index of Steins $(V-R) = 0.52 \pm 0.03$ (Article I) allows us to determine the corresponding ranges for the albedo p_V in the V band: $p_V = 0.26$–0.27, in the first case, and $p_V(H-G) = 0.33$–0.35, in the second case.

3.4. The physical properties of asteroid Steins

Now that we have restricted the range of geometric albedo p_V, we can go back to Fig. 3, and narrow down the determination of the size and of the thermal inertia for a given value of η (hatched region):

- for $\eta = 1.0$: $I \sim 90$ J K^{-1} m^{-2} s$^{-1/2}$, $r_n \sim 2.48$ km;
- for $\eta = 0.9$: $I \sim 140$ J K^{-1} m^{-2} s$^{-1/2}$, $r_n \sim 2.45$ km; and
- for $\eta = 0.8$: $I \sim 210$ J K^{-1} m^{-2} s$^{-1/2}$, $r_n \sim 2.43$ km.

The value of η cannot be independently determined, and we must keep the reasonable range 0.8 to 1.0. We then obtain the following determinations for the physical parameters of Steins:

- $I = 150 \pm 60$ J K^{-1} m^{-2} s$^{-1/2}$;
- $r_n = 2.46 \pm 0.03$ km;
- $p_V = 0.27 \pm 0.01$, $p_R = 0.31 \pm 0.01$; and
- $p_V(H-G) = 0.34 \pm 0.01$, $p_R(H-G) = 0.40 \pm 0.01$.

It must be kept in mind that the geometric albedo is linked to the phase integral q, through the Bong albedo $A = pq$. We use a reasonable value $q = 0.28$ (Sect. 3.2), but a different value would yield different determinations of the albedo. The above uncertainties only reflect the limitations in our modeling method. Other sources of uncertainties must be taken into account:

- the uncertainty in the flux measurements (~15%), which translates into an uncertainty of ~8% on the radius and ~15% on the albedos;
- the uncertainty in the average SED (~3%), which translates into an uncertainty of ~1% on the radius and ~3% in the albedos;
- the uncertainty in the R magnitude (~0.3%) when using the linear phase law, which translates into an uncertainty of 3% in p_R;
- the uncertainty in the R magnitude (~0.6%) when using the (H,G) phase law, which translates into an uncertainty of 7% on $p_R(0)$; and
- the uncertainty in the color index $(V-R)$ (~6%), which translates into an additional uncertainy of 3% on p_V and $p_V(0)$.

The quadratic sum of all the errors leads to the following final uncertainties:

- $I = 150 \pm 60$ J K^{-1} m^{-2} s$^{-1/2}$;
- $r_n = 2.46 \pm 0.20$ km;
- $p_V = 0.27 \pm 0.04$, $p_R = 0.31 \pm 0.05$; and
- $p_V(H-G) = 0.34 \pm 0.06$, $p_R(H-G) = 0.40 \pm 0.07$.

3.5. Solution for the three-dimensional shape

A thermal light curve for asteroid Steins can be constructed by integrating each individual SED between 5 and 33 μm, and plotting the resulting thermal fluxes as a function of time. It is double peaked as illustrated in Fig. 5, consistent with the rotation of an elongated body. Using our solution for the three-dimensional shape of Steins and its rotational state derived from visible observations (Article II), we calculate the corresponding thermal fluxes for the above restricted ranges of parameters. The fit to the data is performed by adjusting the phase shift and the scaling factor γ using a chi-square method.

Figure 5 illustrates the result for the mid-range combination $\eta = 0.9$, $I = 150$ and $p_V = 0.27$. The residuals between the calculated light curve and the data points do not exceed 5%, a highly satisfactory result in view of the complexity of the overall procedure.

The determination of the parameter γ further allows us to scale our three-dimensional model of the shape of Steins, and we find overall dimensions of 5.73 ± 0.52, 4.95 ± 0.45, and 4.58 ± 0.41 km for our nominal solution. The error bars (±~9%) reflect the uncertainties discussed in the above section, not those inherent to the determination of the shape from light curve inversion (see Article II). The radius of the sphere having the same volume (64.3 km^3) is equal to 2.49 km, in excellent agreement with the above determination $r_n = 2.46$ km based on the spherical assumption.

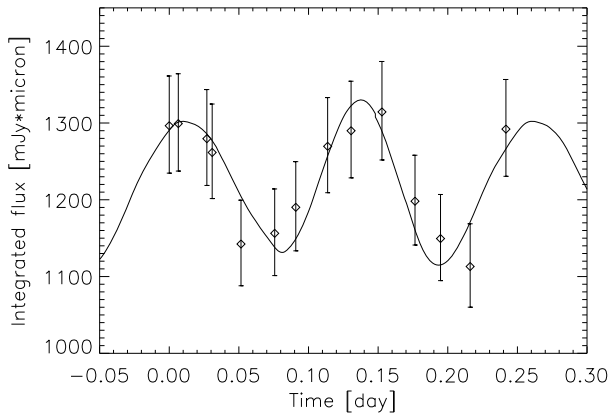

Fig. 5. The thermal light curves of asteroid Steins derived from the SST measurements (diamonds) and from our thermal model with $\eta = 0.9$, $I = 150$ J K^{-1} m^{-2} s$^{-1/2}$ and $p_V = 0.27$ (solid line). The error bars of ±5% are intended to assess the quality of the fit.

4. Conclusions

Our SST observations of asteroid Steins, one of the target of the Rosetta mission, have enabled us to determine its physical properties. Our main findings are summarized below.

1. The solution for a spherical shape leads to an effective radius $r_n = 2.46 \pm 0.20$ km.
2. The thermal inertia amounts to $I = 150 \pm 60$ J K^{-1} m^{-2} s$^{-1/2}$, for a beaming factor between 0.8 and 1.0. This value is consistent with our understanding of E-type asteroids as differentiated bodies having experienced significant heating episodes. To put this result in perspective, it is comparable to the average value of 200 J K^{-1} m^{-2} s$^{-1/2}$ found for Near Earth Asteroids (Delbó et al. 2007), but larger than the typical values of 5−25 J K^{-1} m^{-2} s$^{-1/2}$ found for main belt asteroids (Müller & Lagerros 1998).
3. The geometric albedos are $p_V = 0.27 \pm 0.04$ and $p_R = 0.31 \pm 0.05$, using a linear phase law with $\beta = 0.02$ mag/deg, and $p_V(H-G) = 0.34 \pm 0.06$ and $p_R(H-G) = 0.40 \pm 0.07$, using a (H,G) phase law with $G = 0.35$ mag/deg. As already pointed out by Jorda et al. (2008, Article I), an albedo $p_V(H-G) = 0.34 \pm 0.06$ is somewhat smaller than the other reported values for E-type asteroids, see for instance Belskaya & Shevchenko (2000).
4. The Bong albedo $A_B = pq$ is the parameter that really matters for the thermal balance as seen in Eq. (1) since it expresses the fraction of energy reflected from the surface to that received from the Sun. Assuming that our adopted value for the phase integral $q = 0.28$ is correct, we obtain $A_B = 0.076$ in the V band.
5. Taking into account the respective uncertainties, the results of Fornasier et al. (2006) $p_V = 0.45 \pm 0.1$ and $r_n \sim 2.3$ km are compatible with our results, thus showing that the empirical relationship between albedo and polarization is capable of producing correct estimates.
6. The solution for our 3-dimensional shape model has overall dimensions of 5.73 ± 0.52, 4.95 ± 0.45, and 4.58 ± 0.41 km.

Acknowledgements. This work is based on observations made with the Spitzer Space Telescope, which is operated by the Jet Propulsion Laboratory, California Institute of Technology under a contract with NASA. We thank the SST ground system personnel for their prompt and efficient scheduling of the observations. I. Toth and O. Groussin are supported by grants from CNES (Centre National d'Études Spatiales) for their work at Laboratoire d'Astrophysique de Marseille.

References

Barucci, M. A., Fulchignoni, M., Fornasier, S., et al. 2005, A&A, 430, 313
Barucci, M. A., Fornasier, S., Dotto, E., et al. 2008, A&A, 477, 665 (Article IV)
Belskaya, I. N., & Shevchenko, V. G. 2000, Icarus, 147, 94
Buratti, B. J., Hicks, M. D., Soderblom, L. A., et al. 2004, Icarus, 167, 16
Clark, B. E., Veverka, J., Helfenstein, P., et al. 1999, Icarus, 140, 53
Delbó, M., Harris, A. W., Binzel, R. P., Pravec, P., & Davies, J. K. 2003, Icarus, 166, 116
Delbó, M., Del'Oro, A., Harris, A. W., Mottola, S., & Mueller, M. 2007, Icarus, 190, 236
Fornasier, S., Belskaya, I., Fulchignoni, M., Barucci, M. A., & Barbieri, C. 2006, A&A, 449, L9
Groussin, O., Lamy, P., & Jorda, L. 2004, A&A, 413, 1163
Hanner, M. S., Giese, R. H., Weiss, K., & Zerull, R. 1980, A&A, 104, 42
Harris, A. W. 1998, Icarus, 131, 291
Helfenstein, P., & Veverka, J. 1989, in Asteroids II, ed. R. Binzel, T. Gehrels, & M. S. Matthews (Tucson: Univ. of Arizona Press), 557
Helfenstein, P., Veverka, J., Thomas, P. C., et al. 1996, Icarus, 120, 48
Houck, J. R., Roellig, T. L., & Van Cleve, J. 2004, Proc. SPIE, 5487, 62
Jewitt, D. C. 1991, in Comets in the post-Halley era., ed. R. L. Newburn, M. Neugebauer, & J. Rahe (Dordrecht, Boston, London: Kluwer Acad. Pub.), 19
Jorda, L., Lamy, P., Faury, G., et al. 2008, A&A, 487, 1171 (Article I)
Lagerros, J. S. V. 1998, A&A, 332, 1123
Lamy, P. L., Toth, I., Weaver, H. A., et al. 2006, A&A, 458, 669
Lamy, P. L., Kaasalainen, M., Weissman, P., et al. 2008, A&A, 487, 1179 (Article II)
Lebofsky, L. A., & Spencer, J. R. 1989, in Asteroids II, ed. R. P. Binzel, T. Gehrels, & M. S. Matthews (Tucson: Univ. of Arizona press), 128
Lebofsky, L. A., Sykes, M. V., Tedesco, E. F., et al. 1986, Icarus, 68, 239
Müller, T. G., & Lagerros, J. S. V. 1998, A&A, 338, 340
Russell, H. N. 1916, ApJ, 43, 173
Spencer, J. R., Lebofsky, L. A., & Sykes, M. V. 1989, Icarus, 78, 337
Thomas, P. C., Adinolfi, D., Helfenstein, P., et al. 1996, Icarus, 123, 536
Weissman, P. R., Lowry, S. C., & Choi, Y. J. 2007, A&A, 466, 737
Werner, M. W., Roellig, T. L., Low, F. J., et al. 2004, ApJS, 154, 1